



HAL
open science

Spherulitic crystallization of quartz-like GeO₂ and correlated second harmonic generation in sodium tantalum germanate glasses

Renato Oliveira Evangelista, Thierry Cardinal, Evelyne Fargin, Sonia Buffiere, Nithavong Cam, Marc Dussauze, Vincent Rodriguez, Frederic Adamietz, Lia Marcondes, Gislene Batista, et al.

► To cite this version:

Renato Oliveira Evangelista, Thierry Cardinal, Evelyne Fargin, Sonia Buffiere, Nithavong Cam, et al.. Spherulitic crystallization of quartz-like GeO₂ and correlated second harmonic generation in sodium tantalum germanate glasses. *Journal of Alloys and Compounds*, 2021, 877, pp.160245. 10.1016/j.jallcom.2021.160245 . hal-03257265

HAL Id: hal-03257265

<https://hal.science/hal-03257265v1>

Submitted on 10 Jun 2021

HAL is a multi-disciplinary open access archive for the deposit and dissemination of scientific research documents, whether they are published or not. The documents may come from teaching and research institutions in France or abroad, or from public or private research centers.

L'archive ouverte pluridisciplinaire **HAL**, est destinée au dépôt et à la diffusion de documents scientifiques de niveau recherche, publiés ou non, émanant des établissements d'enseignement et de recherche français ou étrangers, des laboratoires publics ou privés.

Spherulitic crystallization of quartz-like GeO₂ and correlated second harmonic generation in sodium tantalum germanate glasses

Renato Oliveira Evangelista^a, Thierry Cardinal^b, Evelyne Fargin^b, Sonia Buffiere^b, Nithavong Cam^c, Marc Dussauze^d, Vincent Rodriguez^d, Frederic Adamietz^d, Lia Marcondes^a, Gislene Batista^a, Fabia Castro Cassanjes^a, Gael Poirier^{a*}

^a Instituto de Ciência e Tecnologia, Universidade Federal de Alfenas, Poços de Caldas, Minas Gerais CEP 37715-400, Brazil

^b Institut de Chimie de la Matière Condensée de Bordeaux, Université de Bordeaux, 87 Avenue du Dr Schweitzer, Pessac F-33608, France

^c PLACAMAT UMS 3626, Université de Bordeaux, CNRS, 87 Avenue Albert Schweitzer, 3360 Pessac, France

^d Institut des Sciences Moleculaires, UMR 5255, Université de Bordeaux, 351 Cours de la Liberation, Talence Cedex 33405, France

*Correspondence to: Instituto de Ciência e Tecnologia, Cidade Universitária, Campus de Poços de Caldas – UNIFAL-MG, Rodovia José Aurélio Vilela 11999, Poços de Caldas, MG CEP 37715-400, Brazil. / gael.poirier@unifal-mg.edu.br

Abstract

Complex sequential crystallization mechanisms were investigated in the glass composition 70GeO₂-10Na₂O-20Ta₂O₅ prepared by melt-quenching. In a first stage, a classical volume-nucleated crystallization of sodium tantalate perovskite Na₂Ta₈O₂₁ is induced under short time heat-treatments whereas longer annealing treatments promote the formation of surface spherical structures known as spherulites. These singular glass-ceramics were deeply investigated by density measurements, differential scanning calorimetry (DSC), X-ray diffraction (XRD), energy-dispersive X-ray spectroscopy (EDS), Auger Electron Spectroscopy (EDS), correlated Raman and second harmonic generation (SHG) microscopy as well as macro-SHG measurements. These surface spherulites with average size up to 50 μm are richer in tantalum but poorer in germanium than the surrounding material. However, measured SHG signals were found to be related to quartz-like α-GeO₂ grown inside the spherulites. Therefore these materials exhibit a second-order non-linear optical response, related to the symmetry of the point group D₃ given by the quartz GeO₂ grown for the first time in a transparent glass-ceramic.

Keywords : α-GeO₂ / Tantalum / Glass-ceramic / Spherulite / Second harmonic generation

1. Introduction

Glass is usually defined as a non-equilibrium, non-crystalline condensed state of matter that exhibits the glass transition phenomenon and is traditionally obtained by the melt-quenching technique, even though many different synthesis methods are reported [1-4]. Glasses display a key role in modern life because of their outstanding characteristics such as easy synthesis, shape control in pieces or fibers, versatile stoichiometry as well as their ability to transmit, absorb, reflect or scatter electromagnetic radiation depending on the composition, degree of crystallinity and incident wavelength conditions [5-8]. The synergy between all these specific properties makes glasses unique materials for optical applications as either passive or active media. In fact, silica optical fibers are efficient devices for long-distance light transmission with very low attenuation [9]. On the other hand, well-designed glass compositions, usually doped with rare earth active ions, are also able to emit specific wavelengths of technological interest and are applied for optical amplification or glass-based laser cavities [10-12]. Other research field of great interest is related with the non-linear interaction of light with glassy materials, giving rise to non-linear optical responses such as multiphoton absorption or non-linear refractive index [13], [14]. Besides these third order non-linear properties, preliminary suitable treatments of the mother glass can break the glass isotropy and second order non-linear effects such as Second Harmonic Generation (SHG) are promoted. In

practice, these second order responses are usually obtained by optical or electrical poling procedures [15-20] or controlled crystallization of non-centrosymmetric crystalline phases [21-24]. Such glass-ceramics take advantage of the optical properties of the crystalline phase with the overall previously cited characteristics of the precursor glassy phase [25-27].

Glasses based on germanium oxide (glass former) exhibit a broad optical transparency window from 0.35 to 5.5 μm , together with lower processing temperatures when compared with classical silicate glasses [28], [29]. Optical interests on germanate glasses also include lower phonon energy and dispersion constant as well as higher refractive index [30]. Alongside, with the addition of Ta_2O_5 , their thermal stability can be controlled to avoid crystallization over a wide temperature range or to promote precipitation of optically interesting crystalline phases [31-33]. Therefore, since germanate glasses can present high chemical resistance in different environments, simple synthesis and good optical quality, they could be applied for linear and nonlinear optical (NLO) purposes and were already investigated as rare earth hosts and NLO media [32], [34]. As stated before, second order NLO responses are only possible when the glassy material has its intrinsic center of symmetry broken, for example, by the precipitation of non-centrosymmetric crystals from the glass matrix which could create, specifically, second harmonic generation (SHG). However, in order to achieve SHG signals, the crystal growth must be carefully controlled in such a way that the glass ceramic presents intense SHG signal together with a suitable transparency for ONL applications [35-37]. Finally, symmetry aspects explain those optical responses. For example germanium oxide GeO_2 can be present as a glassy material as well as crystalline phases quartz ($\alpha\text{-GeO}_2$ trigonal, $P3121$, $P3221$) or rutile (r-GeO_2 tetragonal, $P42/mnm$) and the final second order NLO response associated with specific anisotropy of each structure [38].

This work is an investigative study on glass ceramics from the $\text{GeO}_2\text{-Ta}_2\text{O}_5\text{-Na}_2\text{O}$ glass system. Crystallization mechanisms were investigated by thermal analysis to define heat-treatment conditions for glass-ceramics production. Density and macroscopic SHG measurements were also performed on these glass-ceramics as a function of the crystallization kinetics. Specific surface spherulites observed after long heat-treatment times were characterized by EDS and Nano Auger elemental analysis. Crystalline phase characterizations were obtained by X-ray diffraction and Raman spectroscopy. Furthermore, the relation between surface spherulites and SHG signals was elucidated through detailed correlated Raman/SHG microscopies.

2. Experimental

2.1. Glasses and glass-ceramics synthesis

The glass samples (labeled G) were prepared by the traditional melt-quenching method with molar composition of $70\text{GeO}_2\text{-}10\text{Na}_2\text{O}\text{-}20\text{Ta}_2\text{O}_5$ out of 20 g in total mass. Each component (GeO_2 , Ta_2O_5 and Na_2CO_3) with high analytical purity reagent grade GeO_2 99.9%, Ta_2O_5 99.9%, and Na_2CO_3 (from Sigma-Aldrich Corp.) were weighted according to the desired molar composition, grinded in an agate mortar and heated for 1 h at 400 $^\circ\text{C}$ to release adsorbed species and then another 1 h at 1500 $^\circ\text{C}$ in a platinum crucible. The crucible bottom, with the final homogeneous melt, was quickly cooled in a tank filled with room temperature water until the inside liquid became a glassy material. Annealing process was performed at 700 $^\circ\text{C}$ for 6 h and the final sample then slowly cooled down to room temperature at 1 $^\circ\text{C}/\text{min}$. The glass samples were optically polished up to around 2 mm in thickness. Glass-ceramics (labeled GC) were obtained from the pristine glass samples by heat treatments at 800 $^\circ\text{C}$ for 1–624 h and labeled according to their specific heat-treatment temperatures and times as follows: GC-T-t, where T is the heat treatment temperature in $^\circ\text{C}$ and t is the time in hours.

2.2. Characterizations

DSC measurements were performed in a Netzsch Calorimeter STA 449 F3 Jupiter in bulk samples of around 40 mg, in a Pt/Rh covered crucible from 200 to 1200 $^\circ\text{C}$, at 10 $^\circ\text{C}/\text{min}$ heating rate under N_2 atmosphere. Densities were measured by the buoyancy method based on the Archimedes Principle and reproduced 5 times for each sample. Silicon dioxide was used as reference and diethyl phthalate density was considered at each measurement according to the experimental temperature. The expression used was $\rho = \rho_d (m_a / (m_a - m_d))$, where ρ = sample

density, m_a = sample weight in air, m_d = sample weight in diethyl phthalate and ρ_d = diethyl phthalate density adjusted at each temperature. For macro-SHG measurements, the laser source was a 10 ns OPO intracavity (Photonics Industry) operating at 1550 nm at a repetition rate of 30 Hz, fundamental unfocused (collimated) beam with a diameter of $\sim 3200 \mu\text{m}$ and incident angle orthogonal to the sample surface with an horizontal polarization for both the incident laser beam and SHG signal detected in transmission mode. All SHG intensities were corrected from the setup conditions (photomultiplier sensitivity) and incident laser intensity ($I_{2\omega}/I_{\omega}^2$). Correlative micro-Raman and micro-SHG measurements were recorded in backscattering mode on a modified micro-Raman spectrometer HR800 (Horiba Jobin-Yvon) at room temperature. A CW laser operating at 532 nm was used for Raman and a picosecond pulsed laser at 1064 nm for micro-SHG measurements. Typical resolution used for Raman is 2.5 cm^{-1} . The microscope objective was a $100\times$ long working distance with a numerical aperture of 0.5 from Mitutoyo, allowing for a resolution in the X–Y plane of $1 \mu\text{m}$ for Raman measurements. Energy-Dispersive X-ray Spectroscopy (EDS) analyzes were carried out with a JEOL SEM (JSM 6360A) with an EDS detector (Si-Li), voltage of 15 kV and working distance of 10 mm. The ϕ - ρ -Z standardless method was employed as a correction for quantitative analysis. Auger Electron Spectroscopy (AES) measurements were performed using a PHI 710 Scanning Auger Nanoprobe. The equipment was set with a field emission source (FEG) as electron gun, coaxial cylindrical micro analyzer and secondary electron detector for imaging. Samples were metallized with Au (3–5 nm) and tilt at 66° to limit charge effects. Few seconds of an argon sputtering ion gun were applied before analyzes to clean the gold and the carbon contamination on the analyzed surface. The maps were obtained at 5 kV with a current of 10 nA. The oxygen, germanium and tantalum were measured with 3 points per peak on the O KLL at 510 eV, the Ge LMM at 1150 eV and the Ta MNN at 1680 eV.

3. Results and discussion

Colorless and homogeneous glass samples of composition 70GeO_2 - $10\text{Na}_2\text{O}$ - $20\text{Ta}_2\text{O}_5$ were obtained by melt-quenching as presented in Table 1. DSC measurements give important informations about glass stability and structural changes in the material such as crystallization mechanisms, among others [39], [40]. The DSC curve of our glass sample presented in Fig. 1 points out a glass transition temperature T_g around 708°C , a onset of the first crystallization event T_{x1} around 800°C and the complete first crystallization temperature T_{c1} around 814°C . Besides this first intense crystallization peak, another weak exothermic event could be detected around 865°C . From a general analysis of these results, one can deduce that this glass composition is relatively stable against devitrification ($T_{x1} - T_g = 92^\circ\text{C}$), which is in agreement with glass formation obtained under relatively slow quenching conditions, but several crystalline phases can be precipitated by heat treatment above 800°C . Since previous works pointed out that increasing Ta_2O_5 contents in alkaline germanate glasses promote higher crystallization tendencies [31], one could note that the low temperature crystalline phase formed by phase separation is related with a tantalum-containing compound. Based on these thermal results, heat treatments were performed at 800°C for times ranging from 1 h to 624 h to produce glass-ceramics as shown for some representative glass-ceramics in Table 1. DSC curves of GC produced after heat-treatments for 1, 20 and 48 h are also resumed in Fig. 1 and give a first insight of the crystallization mechanism: one can observe that the low temperature phase crystallizes within the first hour since the associated exothermic signal is not clearly detected in the glass-ceramic GC-800C-1 h. On the other hand, the crystallization kinetics of the high temperature phase seems to be slower since the corresponding exothermic event is still present after 20 h and apparently disappears after 48 h. The progressive loss of transparency under heat treatment (Table 1) is suggested to be related with both progressive crystallization of the high temperature phase as well as aggregation of the low temperature phase crystallites promoted by a lower viscosity at 800°C and increasing light scattering. For identification of the crystalline phases and a better understanding of the overall crystallization mechanism, X-ray diffraction measurements were performed on the pristine glass and glass-ceramics after heat treatment times ranging from 1 h to 624 h as presented in Fig. 2. The low temperature crystalline phase is attributed to sodium tantalate perovskite of tungsten bronze-like structure $\text{Na}_2\text{Ta}_8\text{O}_{21}$ in agreement with the database reference JCPDS 28-1137. However, this crystallographic reference related with a study devoted to sodium tantalates and oxyfluorotantalates [41] only indexed the diffraction peaks from 10° to 40° but the diffraction positions for higher angles were not reported. In order to use a more accurate comparative diffraction pattern, crystalline powder $\text{Na}_2\text{Ta}_8\text{O}_{21}$ was synthesized by solid state reaction of a 4:1 mixture of Ta_2O_5 and Na_2CO_3 grinded in an agate mortar, compacted in a tablet using a hydraulic press and heat treated at 1400°C for 24 h. As shown in Fig. 2, this powder sample exhibits all the diffraction peaks of reference JCPDS 28-1137 between 10° and 40° together

with other diffraction signals above 40° attributed to the same crystalline phase $\text{Na}_2\text{Ta}_8\text{O}_{21}$. Based on these two X-ray diffraction references, it appears that all diffraction peaks detected in the glass-ceramics match with sodium tantalate $\text{Na}_2\text{Ta}_8\text{O}_{21}$ crystalline phase. One should also note that crystallization of quartz-like $\alpha\text{-GeO}_2$ can be neither excluded nor confirmed at this stage in these glass-ceramics because of the angle position match with sodium tantalate. However, even if the DSC characterization points out the coexistence of at least two crystalline phases for long heat-treatments, no other oxide crystalline phase containing germanium and/or sodium and/or tantalum could be identified from the X-ray diffraction patterns.

Another interesting and unexpected feature detected in these glass-ceramics is related with the formation of surface spherical structures appearing after 18 h and growing for longer heat treatments as presented in Fig. 3 and Table 1. Initially, these spherulites are preferentially formed at the corners and surface defects of the sample (Fig. 3a). However, under longer heat treatment they spread all over the surface, along with a spherulite radius increase (Fig. 3c–f). Spherulites detected after 18 h at 800°C display an average radius of $9\ \mu\text{m}$ but keep growing linearly rather than exponentially as a function of time as shown in Fig. 4a and then stabilize at around $50\ \mu\text{m}$. Indeed, spherulite features usually present a linear radius growth for constant temperatures until their growth is stopped by impingement with neighboring spherulites forming polyhedral structures as highlighted in Fig. 3c, e and f [42]. It is also suggested that they could be originated by fibrillar crystals in the center, where the “nucleation” of the spherulites initiates [42]. Therefore, spherulites with the same radius size seems to nucleate simultaneously [43], [44]. Finally, one can notice that the spherical growth occurs until spherulites come into contact after which a coalescence process with well-defined boundaries is observed according to the Fig. 3e and f. Furthermore, overall density of the samples increases with HT time (Fig. 4b). The glass presents a high density of $5.21\ \text{g/cm}^3$, in agreement with the relatively high atomic mass of the main elements Ta and Ge. The density increases until 624 h and gives a value of $5.46\ \text{g/cm}^3$. This density growth is foreseen and related to the better atomic arrangement due to crystallization. For the same composition, it is expected that the stable crystalline phase has a lower free energy and then higher density than a metastable glassy phase [45].

These glass-ceramics and their detailed spherulitic crystallization mechanisms displayed a strong interest after the evidence of second harmonic generation (SHG) whose intensity depends on the crystallization conditions as resumed in Table 1 and Fig. 4a for representative samples. In fact, no SHG signals could be detected in the pristine glass nor glass-ceramics until 18 h of heat treatment using our macro-SHG set up. At this point, a weak SHG response was collected in sample GC-800C-18 h, which is also the sample with the lowest heat treatment time presenting surface spherulites. Other SHG measurements recorded on a sample with well-formed spherulites (GC-800C-72 h) displayed stronger SHG signals with an increase of two order of magnitude. For the sample treated during 624 h, the SHG signal is about 10^6 stronger under our measurement conditions. These data highlight a need for a detailed spherulite characterization and a coherent correlation with the SHG signals.

For a better understanding of the spherulite formation, structure and composition, elemental analyzes were also performed by EDS (Energy Dispersive X-ray Spectroscopy) and AES (Auger electron Spectroscopy) in samples GC-800C-18 h and GC-800C-72 h (Fig. 5, Fig. 6 and Table 2). These measurements were realized on slightly polished surfaces in order to eliminate any glass boundaries as well as for a better analysis of the spherulites. Results obtained on sample GC-800C-18 h are related with spherulites in their early formation stage whereas sample GC-800C-72 h contains well-formed and grown spherulites. In this sense, the EDS data from Fig. 5 and Table 2 clearly point out that spherulite formation is spatially correlated with a higher tantalum and lower germanium content than the surrounding (outside area). Quantitative data concerning sodium were considered constant along the whole surface within the experimental error. These quantitative analyzes are a first indication that spherulite formation is in some extent related with a phase separation between a tantalum-rich and germanium-rich phase. Another important point concerning spherulite droplet-like formation is related with their crystalline and/or amorphous nature. Whereas several reports attributed spherulites to monocrystals, other works identified that spherulitic structures are only partially crystalline and formed from fibrillar crystals grown from a nucleus embedded in a glassy-like phase [46], [47]. Some works even attributed the structure of spherulites to “anti-glass” networks [48]. In our case, the spherulites cannot be attributed to single crystals of sodium tantalate because of the still high germanium content detected by EDS (spatial resolution of $1\ \mu\text{m}^3$). Once EDS could not bring further information about oxygen tendency, AES analyzes were performed on both GC-800C-18 h and GC-800C-72 h to probe relative elemental analysis of both Ta, Ge and O as detailed in Fig. 6. Quantitative results for

Ta and Ge are in agreement with EDS data concerning a progressive higher tantalum and lower germanium content inside the spherulites when compared to the outside surrounding area. This behavior can be understood as a phase separation mechanism with spherulites formed from richer tantalum and poorer germanium contents. In other words, the spherulite formation is related with a microscale migration of tantalum in spherical areas whereas germanium follows an opposite trend. However, one should note that a classical amorphous phase separation cannot fully describe the spherulite formation since this event is taking place in an already formed glass-ceramic containing $\text{Na}_2\text{Ta}_8\text{O}_{21}$ crystallites. On the other hand, relative oxygen quantification follows a quite unexpected trend since the oxygen seems to be slightly lower in the spherulites. Another correlated information is that germanium contrast is not detected during the formation of spherulites (Fig. 6b) but only for longer heat treatments (Fig. 6f). Based on these elemental analyzes, one could infer that long heat treatments above the glass transition temperature promote the diffusion of tantalum species (from crystalline $\text{Na}_2\text{Ta}_8\text{O}_{21}$ and/or from the remaining glassy phase) and their concentration in localized spherical areas (spherulites). This tantalum diffusion induces in a second step the opposite diffusion of germanate species out of these spherulites.

Correlative Raman and SHG microscopies were performed on samples GC-800C-18 h and GC-800C-72 h (Table 3, Table 4) and representative Raman spectra were extracted from these 2D mappings as presented in Fig. 7. The first key information highlighted in Table 3, Table 4 is that SHG signals are only generated from the spherulites but the surrounding areas are not SHG active as suspected earlier by the appearance of macro-SHG signals only after heat-treatment for at least 18 h. Raman spectra extracted from 2D Raman mappings inside and outside of the spherulites for both samples were also compared with quartz-like $\alpha\text{-GeO}_2$ and crystalline $\text{Na}_2\text{Ta}_8\text{O}_{21}$.

For quartz-like GeO_2 , Raman bands attribution is well-known and reported elsewhere [49]: the germanium atoms are located at the center of corner-shared GeO_4 tetrahedra, resulting in the following irreducible representation of optical vibrations: $G = 4A_1 + 4A_2 + 8E$ with A_1 modes being Raman active, A_2 modes IR active and E modes both Raman and IR active. Hence, degenerated E modes may also split in TO and LO modes. Table 5 gives a detailed attribution of the detected Raman bands of $\alpha\text{-GeO}_2$. A careful analysis of the Raman spectrum for $\text{Na}_2\text{Ta}_8\text{O}_{21}$ is also needed for a better understanding of the glass-ceramics structural behavior. This Raman spectrum has never been reported for this sodium tantalate phase but XRD studies elucidated structural peculiarities of this perovskite phase [41].

Its crystalline structure is similar to tetragonal tungsten bronze $\text{K}_{0.6}\text{WO}_3$ but additional weak diffraction peaks are in agreement with the existence of a superstructure and tripling of parameter b . The crystalline network is built from corner-shared TaO_6 octahedra in a way that free-space cavities are also formed between this octahedral framework being larger cavities labeled A_1 and A_2 of coordination 12 and 15 and smaller B cavities of coordination 9. A_1 and A_2 cavities are located one above the other along the c axis forming tunnels where large cations like sodium or potassium can be accommodated. According to tungsten bronzes structures, the general compound formula should be $(A_1)_2(A_2)_4B_4M_{10}O_{30}$ but the tripling of parameter b implies a corrected formula being $(A_1)_6(A_2)_{12}B_{12}M_{30}O_{90}$. However, density measurements of 7.56 ± 0.03 give for the orthorhombic cell the statistical formula: $\text{Na}_9\text{Ta}_{36}\text{O}_{94.5}$, justifying the hypothesis that 6 sodium are found in A_1 cavities and the exceeding 3 sodium, 6 tantalum and 4.5 oxygens atoms in the A_2 cavities where Ta and O form linear $(\text{Ta}_4\text{O}_3)_n$ chains inserted inside the A_2 tunnels along the c axis [41]. Thus, the overall formula can be represented by: $\text{Na}_6[\text{Na}_3(\text{Ta}_4\text{O}_3)_{3/2}]\text{Ta}_{30}\text{O}_{90}$. As a consequence, two completely different Ta–O bonds are present in $\text{Na}_2\text{Ta}_8\text{O}_{21}$: Ta–O bonds from the corner-shared TaO_6 framework and Ta–O bonds from the linear chains Ta_4O_3 inside the A_2 tunnels. Based on these considerations, it is suggested that the Raman signal at lower frequency (557 cm^{-1}) is related with Ta–O–Ta stretchings from the TaO_6 skeleton whereas the high frequency signal at 665 cm^{-1} is due to Ta–O–Ta stretching of the linear chains in A_2 tunnels (gray arrows in Fig. 7). In the glass-ceramics, these Raman bands are also detected but with a frequency shift of Ta–O stretchings in TaO_6 from 557 cm^{-1} in pure $\text{Na}_2\text{Ta}_8\text{O}_{21}$ to 580 cm^{-1} in the glass-ceramics related with the germanate neighborhood of these tantalate structures. The other signal is not affected by the germanate surrounding since the Ta_4O_3 chains are shielded inside the A_2 tunnels.

For the glass-ceramics, intense and sharp Raman modes are progressively identified inside the spherulites as detailed in Fig. 7 by the black arrows. Although only three modes centered at 120 , 165 and 440 cm^{-1} are detected in sample GC-800C-18 h, other Raman modes are also identified at 260 , 513 and 880 cm^{-1} in sample GC800C-72 h. Two Raman spectra of the inside zone are presented for this last sample since it has been observed that

some modes are excludent i.e. modes at 120 and 165 cm^{-1} are only observed in some areas inside the spherulite where complementary modes at 260 and 880 cm^{-1} are not present. By comparing these spherulite sharp Raman modes with crystalline references, all these signals are undoubtedly related with trigonal (hexagonal) quartz-like $\alpha\text{-GeO}_2$ as previously suspected by XRD analysis [49], [50]. Based on these results, it also appears that crystalline $\alpha\text{-GeO}_2$ is formed only inside the spherulites. To go in more detail, one can focus on the correlative SHG/Raman mapping reported for the larger spherulite (sample GC800C-72 h) and depicted in Table 4. One can notice that (i) SHG signals seem to be spatially correlated with areas where E Raman modes of $\alpha\text{-GeO}_2$ are detected with a higher intensity and (ii) the A_1 and E Raman modes are spatially uncorrelated. A_1 modes at 260 and 880 cm^{-1} are more active along the vertical diameter of the spherulite i.e. a direction parallel to the incident light polarization; whereas both SHG active area and E Raman modes are preferentially observed on the left and right corner of the spherulite i.e. when the diameter of the spherulite is perpendicular to the incident laser polarization. According to the quartz-like $\alpha\text{-GeO}_2$ (D_3 point group) which crystalline structure is set as a positive uniaxial trigonal crystal, having a space group $P3121$ or $P3221$ [38], [51], both E Raman modes and the most intense $\chi^{(2)}$ coefficients are expected for an excitation perpendicular to the trigonal c axis [49]. Thus, both Raman and SHG data are in agreement with the D_3 point group of $\alpha\text{-GeO}_2$ and one can deduce from the correlative maps in Table 4 a spatial distribution of the crystallites which tends to be radial with the spherulite growth. Finally, such observation can partially explain the strong SHG increase (6 order of magnitude) observed with the heat treatment time. As the spherulite size increase, we note a better radial distribution of the SHG active $\alpha\text{-GeO}_2$ crystallites, this better arrangement of the crystallites within domains much larger than both the SHG coherence length and the wavelength was already found to be a key point for such SHG active glass ceramics containing spherulites [36], [37]. In addition, since the 480 cm^{-1} signal ascribed to vitreous germanate network (green arrow in Fig. 7) is detected only out of the spherulites, one could infer that the vitreous germanate network has been disrupted inside the spherulites and may be at the origin $\alpha\text{-GeO}_2$ crystallization.

All these thermal, elemental and spectroscopic data obtained for the pristine glass and glass-ceramics inside and outside the spherulites bring a reasonable overview of the overall crystallization mechanisms and spherulite formation: it is suggested that the glass-ceramic material out of the spherulites is constituted of a glassy sodium tantalum-germanate phase with embedded $\text{Na}_2\text{Ta}_8\text{O}_{21}$ nanocrystals whereas the spherulites are mainly constituted of a comparatively higher content of $\text{Na}_2\text{Ta}_8\text{O}_{21}$ crystallites together with crystals of quartz-like $\alpha\text{-GeO}_2$. Identification of broad Raman signals in the ranges 150–360 cm^{-1} and 500–850 cm^{-1} also suggests a residual glassy phase, even if our data are not fully conclusive for such statement. Since tantalum content is higher and germanium content lower in the spherulite when compared to the surrounding, a first reliable hypothesis is that sodium and tantalum which were initially homogeneously distributed throughout the glass volume migrate toward specific areas next to the surface and aggregate to larger crystallites. In these regions, such progressive growth of sodium tantalate crystallites partially depolymerizes the germanate covalent network and promotes short germanate chains which are the basic units for growth of fibrillar $\alpha\text{-GeO}_2$ crystals forming the spherulites. Such model is consistent with the long heat-treatment times required for spherulite formation triggered by low atomic diffusion rates in such high viscosity conditions.

4. Conclusion

Crystallization mechanisms were investigated in sodium tantalum germanate glasses and were found to be governed by precipitation of bronze-like perovskite nanocrystals $\text{Na}_2\text{Ta}_8\text{O}_{21}$ at 800 °C (onset of low temperature crystallization event) whereas longer heat-treatments give rise to the formation of spherulitic structures responsible for Second Harmonic Generation (SHG). Correlated Raman and SHG microscopy allowed to determine that trigonal quartz-like $\alpha\text{-GeO}_2$ is produced under heat-treatment inside the spherulites and is suggested to be at the origin of the SHG signals. Quantitative elemental analyzes also identified a lower germanium and higher tantalum content inside these spherical structures and these data were used to understand the spherulite formation. To our knowledge, this is the first report of transparent glass-ceramics containing SHG active $\alpha\text{-GeO}_2$ crystals.

Credit authorship contribution statement

Renato Oliveira Evangelista: Methodology, Formal analysis, Investigation, Data curation, Writing - original draft. **Thierry Cardinal:** Conceptualization, Formal analysis, Investigation, Resources, Data curation, Supervision, Writing - original draft, Funding acquisition. **Evelyne Fargin:** Investigation, Resources, Data curation. **Sonia Buffière:** Methodology, Formal analysis, Data curation. **Nithavong Cam:** Methodology, Formal analysis, Data curation. **Marc Dussauze:** Methodology, Formal analysis, Investigation, Resources, Writing - original draft, supervision. **Vincent Rodriguez:** Methodology, Formal analysis, Investigation, Resources, Supervision. **Frédéric Adamietz:** Methodology, Formal analysis. **Lia Marcondes:** Formal analysis, Data curation, Writing - original draft. **Gislene Batista:** Formal analysis, Data curation, Writing - original draft. **Fabia Castro Cassanjes:** Methodology, Validation, Data curation, Project administration. **Gael Poirier:** Conceptualization, Methodology, Validation, Formal analysis, Investigation, Resources, Data curation, Writing - original draft, Writing - review & editing, Supervision, Project administration, Funding acquisition.

Declaration of competing interest

The authors declare that they have no known competing financial interests or personal relationships that could have appeared to influence the work reported in this paper.

Acknowledgments

The authors would like to thank Brazilian funding agencies Conselho Nacional de Desenvolvimento Científico e Tecnológico – CNPq, Fundação de Amparo à Pesquisa do estado de Minas Gerais – FAPEMIG, Financiadora de Estudos e Projetos – FINEP, Coordenação de Aperfeiçoamento do Pessoal de Nível Superior – CAPES, for financial support. This research was also supported by the IdEx Bordeaux and the Région Nouvelle Aquitaine. This project has received funding from the European Union’s Horizon 2020 research program under the Marie Skłodowska-Curie Grant agreement No. 823941 (FUNGLASS).

Raman and SHG experiments have been performed at the platform SIV at the University of Bordeaux, funded by the FEDER and the Region Aquitaine.

References

1. C.B. Carter, M.G. Norton. **Glass and glass-ceramics**. C.B. Carter, M.G. Norton (Eds.), Ceramic Materials, Springer, New York (2007), pp. 379-399, [10.1007/978-0-387-46271-4_21](https://doi.org/10.1007/978-0-387-46271-4_21)
2. Z.H. Jiang, Q.Y. Zhang. **The formation of glass: a quantitative perspective**. Sci. China Mater., 58 (2015), pp. 378-425, [10.1007/s40843-015-0048-z](https://doi.org/10.1007/s40843-015-0048-z)
3. E.D. Zanotto, J.C. Mauro. **The glassy state of matter: its definition and ultimate fate**. J. Non-Cryst. Solids, 471 (2017), pp. 490-495, [10.1016/j.jnoncrysol.2017.05.019](https://doi.org/10.1016/j.jnoncrysol.2017.05.019)
4. E.D. Zanotto, F.A.B. Coutinho. **How many non-crystalline solids can be made from all the elements of the periodic table?** J. Non-Cryst. Solids, 347 (2004), pp. 285-288, [10.1016/j.jnoncrysol.2004.07.081](https://doi.org/10.1016/j.jnoncrysol.2004.07.081)
5. J.E. Shelby. Introduction to Glass Science and Technology (second ed.), Royal Society of Chemistry, London (2005).
6. R.H. Doremus. Glass Science (second ed.), John Wiley and Sons, New York (1994).
7. Varshneya, J.C. Mauro. Fundamentals of Inorganic Glasses (third ed.), Elsevier, New York (2019).
8. J.D. Musgraves, J. Hu, L. Calvez. **Springer Handbook of Glass**. Springer, Cham, New York (2019), [10.1007/978-3-319-93728-1](https://doi.org/10.1007/978-3-319-93728-1)
9. M.J. Li, T. Hayashi. **Advances in low-loss, large-area, and multicore fibers**. A.E. Wilner (Ed.), Optical Fiber Telecommunications VII, Academic Press, Cambridge (2020), pp. 3-50, [10.1016/b978-0-12-816502-7.00001-4](https://doi.org/10.1016/b978-0-12-816502-7.00001-4)

10. J. Lucas, P. Lucas, T. Le Mercier, A. Rollat, W. Davenport. **Rare earth doped lasers and optical amplifiers.** In : J. Lucas, P. Lucas, T. Le Mercier, A. Rollat, W. Davenport (Eds.), Rare Earths: Science, Technology, Production and Use, Elsevier, New York (2015), pp. 319-332, [10.1016/B978-0-444-62735-3.00016-4](https://doi.org/10.1016/B978-0-444-62735-3.00016-4)
11. N.G. Boetti, D. Pugliese, E.C. Ginistrelli, J. Lousteau, D. Janner, D. Milanese. **Highly doped phosphate glass fibers for compact lasers and amplifiers: a review.** Appl. Sci., 7 (2017), p. 1295, [10.3390/app7121295](https://doi.org/10.3390/app7121295)
12. M. He, J. Jia, J. Zhao, X. Qiao, J. Du, X. Fan. **Glass-ceramic phosphors for solid state lighting: a review.** Ceram. Int., 47 (2021), pp. 2963-2980, [10.1016/j.ceramint.2020.09.227](https://doi.org/10.1016/j.ceramint.2020.09.227)
13. A.S.S. Reddy, J. Jedryka, K. Ozga, V.R. Kumar, N. Purnachand, I.V. Kityk, N. Veeraiah. **Laser stimulated third harmonic generation studies in ZnO–Ta₂O₅–B₂O₃ glass ceramics entrenched with Zn₃Ta₂O₈ crystal phases.** Opt. Mater., 76 (2018), pp. 90-96, [10.1016/j.optmat.2017.12.030](https://doi.org/10.1016/j.optmat.2017.12.030)
14. A.H. Reshak, O.S. Klymovych, G.L. Myronchuk, O.V. Zamuruyeva, O.F. Zmiy, Z.A. Alahmed, H. Kamarudin. **Glass formation and the third harmonic generation of Cu₂Se–GeSe₂–As₂Se₃ glasses.** J. Appl. Phys., 116 (2014), Article 143102, [10.1063/1.4897457](https://doi.org/10.1063/1.4897457)
15. Y. Quiquempois, N. Godbout, S. Lacroix. **Model of charge migration during thermal poling in silica glasses: evidence of a voltage threshold for the onset of a second-order nonlinearity.** Phys. Rev. A, 65 (2002), Article 043816, [10.1103/PhysRevA.65.043816](https://doi.org/10.1103/PhysRevA.65.043816)
16. X.M. Liu, M.D. Zhang. **Theoretical study for thermal/electric field poling of fused silica.** Jpn. J. Appl. Phys., 40 (2001), pp. 4069-4076, [10.1143/JJAP.40.4069](https://doi.org/10.1143/JJAP.40.4069)
17. M. Dussauze, T. Cremoux, F. Adamietz, V. Rodriguez, E. Fargin, G. Yang, T. Cardinal. **Thermal poling of optical glasses: mechanisms and second-order optical properties.** Int. J. Appl. Glass Sci., 3 (2012), pp. 309-320, [10.1111/ijag.12001](https://doi.org/10.1111/ijag.12001)
18. M. Dussauze, T. Cardinal. **Nonlinear optical properties of glass.** J.D. Musgraves, J. Hu, L. Calvez (Eds.), Handbook of Glass, Springer, Cham, New York (2019), pp. 193-225, [10.1007/978-3-319-93728-1_6](https://doi.org/10.1007/978-3-319-93728-1_6)
19. Y. Sasaki, Y. Ohmori. **Phase-matched sum-frequency light generation in optical fibers.** Appl. Phys. Lett., 39 (1981), pp. 466-468, [10.1063/1.92775](https://doi.org/10.1063/1.92775)
20. W. Margulis, F. Laurell, B. Lesche. **Imaging the nonlinear grating in frequency doubling fibres.** Nature, 378 (1995), pp. 699-701, [10.1038/378699a0](https://doi.org/10.1038/378699a0)
21. Y. Takahashi, Y. Benino, T. Fujiwara, T. Komatsu. **Second harmonic generation in transparent surface crystallized glasses with stillwellite-type LaBGeO₅.** J. Appl. Phys., 89 (2001), pp. 5282-5287, [10.1063/1.1360699](https://doi.org/10.1063/1.1360699)
22. C.A.C. Feitosa, V.R. Mastelaro, A.R. Zanatta, A.C. Hernandes, E.D. Zanotto. **Crystallization, texture and second-harmonic generation in TiO₂-BaO-B₂O₃ glasses.** Opt. Mater., 28 (2006), pp. 935-943, [10.1016/j.optmat.2005.05.003](https://doi.org/10.1016/j.optmat.2005.05.003)
23. N. Maryama, T. Honma, T. Komatsu. **Morphology design of highly oriented nonlinear optical Ba₂TiSi₂O₈ crystals at the glass surface by crystallization in reduced atmosphere.** Opt. Mater., 32 (2009), pp. 35-41, [10.1016/j.optmat.2009.05.014](https://doi.org/10.1016/j.optmat.2009.05.014)

24. H. Masai, S. Tsuji, T. Fujiwara, Y. Benino, T. Komatsu. **Structure and non-linear optical properties of BaO–TiO₂–SiO₂ glass containing Ba₂TiSi₂O₈ crystal.** J. Non-Cryst. Solids, 353 (2007), pp. 2258-2262, [10.1016/j.jnoncrysol.2007.03.005](https://doi.org/10.1016/j.jnoncrysol.2007.03.005)
25. J. Deubener, M. Allix, M.J. Davis, A. Duran, T. Höche, T. Honma, S. Zhou. **Updated definition of glass-ceramics.** J. Non-Cryst. Solids, 501 (2018), pp. 3-10, [10.1016/j.jnoncrysol.2018.01.033](https://doi.org/10.1016/j.jnoncrysol.2018.01.033)
26. W. Höland. *Glass-Ceramic Technology* (second ed.), John Wiley & Sons, Hoboken (2012), [10.1002/9781118265987](https://doi.org/10.1002/9781118265987)
27. Alekseeva, O. Dymshits, M. Tsenter, A. Zhilin, V. Golubkov, I. Denisov, K. Yumashev. **Optical applications of glass-ceramics.** J. Non-Cryst. Solids, 356 (2010), pp. 52-54, [10.1016/j.jnoncrysol.2010.05.103](https://doi.org/10.1016/j.jnoncrysol.2010.05.103)
28. S.S. Bayya, J.S. Sanghera, I.D. Aggarwal. **Infrared transparent germanate glass-ceramics.** J. Am. Ceram. Soc., 85 (2002), pp. 3114-3116, [10.1111/j.1151-2916.2002.tb00594.x](https://doi.org/10.1111/j.1151-2916.2002.tb00594.x)
29. O.L.G. Alderman, A.C. Hannon, S. Feller, R. Beanland, D. Holland. **The germanate anomaly in alkaline earth germanate glasses.** J. Phys. Chem. C, 121 (2017), pp. 9462-9479, [10.1021/acs.jpcc.6b12372](https://doi.org/10.1021/acs.jpcc.6b12372)
30. N. Nagano, M. Saito, M. Miyagi. **Refractive-indexes of SiO₂-based and GeO₂-based glasses near the infrared-absorption peaks.** J. Non-Cryst. Solids, 135 (1991), pp. 114-121, [10.1016/0022-3093\(91\)90411-X](https://doi.org/10.1016/0022-3093(91)90411-X)
31. G.M. De Pietro, C. Pereira, R.R. Gonçalves, S.J.L. Ribeiro, C.D. Freschi, F.C. Cassanjes, G.Y. Poirier. **Thermal, structural, and crystallization properties of new tantalum alkali-germanate glasses.** J. Am. Ceram. Soc., 98 (2015), pp. 2086-2093, [10.1111/jace.13555](https://doi.org/10.1111/jace.13555)
32. L.F. Guedes, L.M. Marcondes, R. Evangelista, G. Batista, V.G. Mendoza, F.C. Cassanjes, G.Y. Poirier. **Effect of alkaline modifiers on the structural, optical and crystallization properties of niobium germanate glasses and glass-ceramics.** Opt. Mater., 105 (2020), Article 109866, [10.1016/j.optmat.2020.109866](https://doi.org/10.1016/j.optmat.2020.109866)
33. C.R. Da Cunha, S.A. Maestri, B.P. De Sousa, L.M. Marcondes, R.R. Gonçalves, F.C. Cassanjes, G.Y. Poirier. **Alkali metal tantalum germanate glasses and glass-ceramics formation.** J. Non-Cryst. Solids, 499 (2018), pp. 401-407, [10.1016/j.jnoncrysol.2018.07.059](https://doi.org/10.1016/j.jnoncrysol.2018.07.059)
34. G.Y. Poirier, M. Dussauze, V. Rodriguez, F. Adamietz, L. Karam, T. Cardinal, E. Fargin. **Second harmonic generation in sodium tantalum germanate glasses by thermal poling.** J. Phys. Chem. C, 123 (2019), pp. 26528-26535, [10.1021/acs.jpcc.9b08221](https://doi.org/10.1021/acs.jpcc.9b08221)
35. H. Vigouroux, E. Fargin, A. Fargues, B. Le Garrec, M. Dussauze, V. Rodriguez, F. Adamietz, Grigoris Mountrichas, E.I. Kamitsos, J.S. Lotarev, V. Sigaev. **Crystallization and second harmonic generation of lithium niobium silicate glass-ceramics.** J. Am. Ceram. Soc., 94 (2011), pp. 2080-2086, [10.1111/j.1551-2916.2011.04416.x](https://doi.org/10.1111/j.1551-2916.2011.04416.x)
36. H. Vigouroux, E. Fargin, S. Gomez, B. Le Garrec, G. Mountrichas, J.E. Kamitsos, M. Dussauze, F. Adamietz, V. Rodriguez. **Synthesis and multiscale evaluation of LiNBO₃-containing glass-ceramics with efficient isotropic SHG response.** Adv. Funct. Mater., 22 (2012), pp. 3985-3993, [10.1002/adfm.201200651](https://doi.org/10.1002/adfm.201200651)

37. L.N. Truong, M. Dussauze, E. Fargin, L. Santos, H. Vigouroux, A. Fargues, F. Adamietz, V. Rodriguez. **Isotropic octupolar second harmonic generation response in LaBGeO₅ glass-ceramic with spherulitic precipitation.** Appl. Phys. Lett., 106 (2015), Article 161901, [10.1063/1.4918808](https://doi.org/10.1063/1.4918808)
38. Kawamura, K. Imakita, A. Kitao, M. Fujii. **Polarization-sensitive second harmonic generation microscopy of α -quartz like GeO₂ (α -GeO₂) polycrystal.** J. Phys. D Appl. Phys., 47 (2014), Article 455305, [10.1088/0022-3727/47/45/455305](https://doi.org/10.1088/0022-3727/47/45/455305)
39. W. Hofstetter, H. Sassik, R. Grössinger, R. Trausmuth, G. Vertesy, L.F. Kiss. **Determination of the onset of crystallization of amorphous materials using different methods.** Mater. Sci. Eng. A Struct., 226–228 (1997), pp. 213-217, [10.1016/S0921-5093\(96\)10620-1](https://doi.org/10.1016/S0921-5093(96)10620-1)
40. B.D. Sanditov, S.S. Sangadiev, D.S. Sanditov. **Relaxation time and cooling rate of a liquid in the glass transition range.** Glass Phys. Chem., 33 (2007), pp. 445-454, [10.1134/S1087659607050021](https://doi.org/10.1134/S1087659607050021)
41. J.P. Chaminade, M. Pouchard, P. Hagenmuller. **Tantalates and oxyfluorotantalates of sodium.** Rev. Chem. Miner., 9 (1972), p. 381. <https://hal.archives-ouvertes.fr/hal-00125096>
42. J. Varga. **Supermolecular structure of isotactic polypropylene.** J. Mater. Sci., 27 (1992), pp. 2557-2579, [10.1007/BF00540671](https://doi.org/10.1007/BF00540671)
43. M. Raimo. **Growth of spherulites: foundation of the DSC analysis of solidification.** ChemTexts, 1 (2015), p. 13, [10.1007/s40828-015-0013-1](https://doi.org/10.1007/s40828-015-0013-1)
44. T. Karasawa, Y. Taketomi. **Growth and structure of spherulites in polymer-dispersed liquid crystals fabricated by photopolymerization-induced phase separation.** Jpn. J. Appl. Phys., 37 (1998), pp. 4448-4453, [10.1143/JJAP.37.4448](https://doi.org/10.1143/JJAP.37.4448)
45. Karamanov, M. Pelino. **Evaluation of the degree of crystallization in glass-ceramics by density measurements.** J. Eur. Ceram. Soc., 19 (1999), pp. 649-654, [10.1016/S0955-2219\(98\)00226-X](https://doi.org/10.1016/S0955-2219(98)00226-X)
46. S.W. Freiman, G.Y. Onoda, A.G. Pincus. **Spherulitic crystallization in glasses.** Am. Ceram. Soc. Bull., 50 (1971), p. 414.
47. P.R. Carpenter, M. Campbell, R.D. Rawlings. **Spherulitic growth of apatite in a glass ceramic system.** J. Mater. Sci. Lett., 5 (1986), pp. 1309-1312, [10.1007/BF01729402](https://doi.org/10.1007/BF01729402)
48. Bertrand, J. Carreaud, G. Delaizir, M. Shimoda, J.R. Duclère, M. Colas, M. Belleil, J. Cornette, T. Hayakawa, C. Genevois, E. Veron, M. Allix, S. Chenu, F. Brisset, P. Thomas. **New transparent glass-ceramics based on the crystallization of “anti-glass” spherulites in the Bi₂O₃-Nb₂O₅-TeO₂ system.** Cryst. Growth Des., 15 (2015), pp. 5086-5096, [10.1021/acs.cgd.5b01048](https://doi.org/10.1021/acs.cgd.5b01048)
49. T.P. Mernagh, L.G. Liu. **Temperature dependence of Raman spectra of the quartz- and rutile-types of GeO₂.** Phys. Chem. Miner., 24 (1997), pp. 7-16, [10.1007/s002690050012](https://doi.org/10.1007/s002690050012)
50. M. Madon, P. Gillet, C. Julien, G.D. Price. **A vibrational study of phase transitions among the GeO₂ polymorphs.** Phys. Chem. Miner., 18 (1991), pp. 7-18, [10.1007/BF00199038](https://doi.org/10.1007/BF00199038)
51. M. Micoulaut, L. Cormier, G.S. Henderson. **The structure of amorphous, crystalline and liquid GeO₂.** J. Phys. Condens. Matter, 18 (2006), pp. 753-784, [10.1088/0953-8984/18/45/R01](https://doi.org/10.1088/0953-8984/18/45/R01)

Figures and Tables

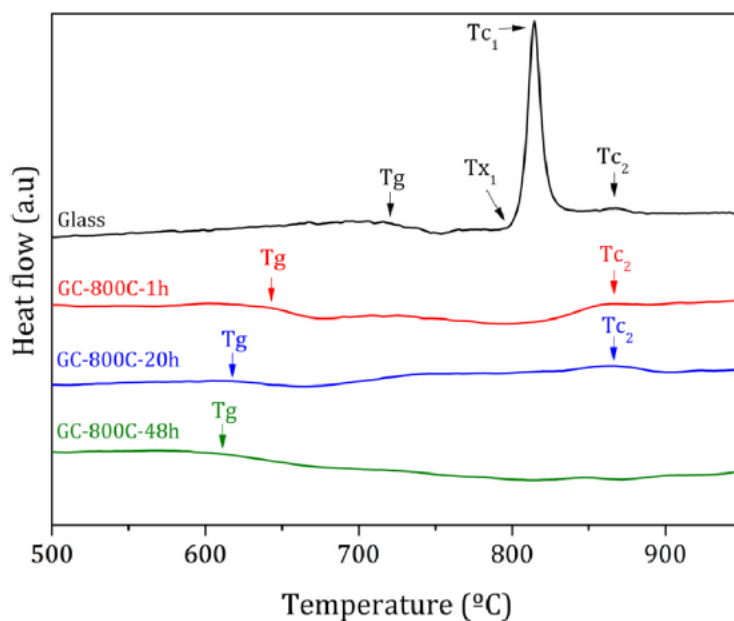







Fig. 1. DSC curves of glass sample of composition $70\text{GeO}_2\text{-}10\text{Na}_2\text{O-}20\text{Ta}_2\text{O}_5$ and corresponding glass-ceramics after heat-treatment at $800\text{ }^\circ\text{C}$ for 1 h, 20 h and 48 h.

Table 1

Spherulite average radius, SHG relative intensity and visual aspect as a function of heat treatment temperature and time for glass (G) and glass-ceramics (GC-T-t).

Sample	G	GC-800C-8h	GC-800C-18h	GC-800C-72h	GC-800C-624h
Heat treatment temperature ($^\circ\text{C}$)	-	800	800	800	800
Heat treatment time (h)	-	8h	18h	72h	624h
Spherulite average radius (μm)	-	-	9	40	50
SHG relative intensity	0	0	Very weak (10^{-5})	Weak (10^{-3})	Strong (10)
Aspect					

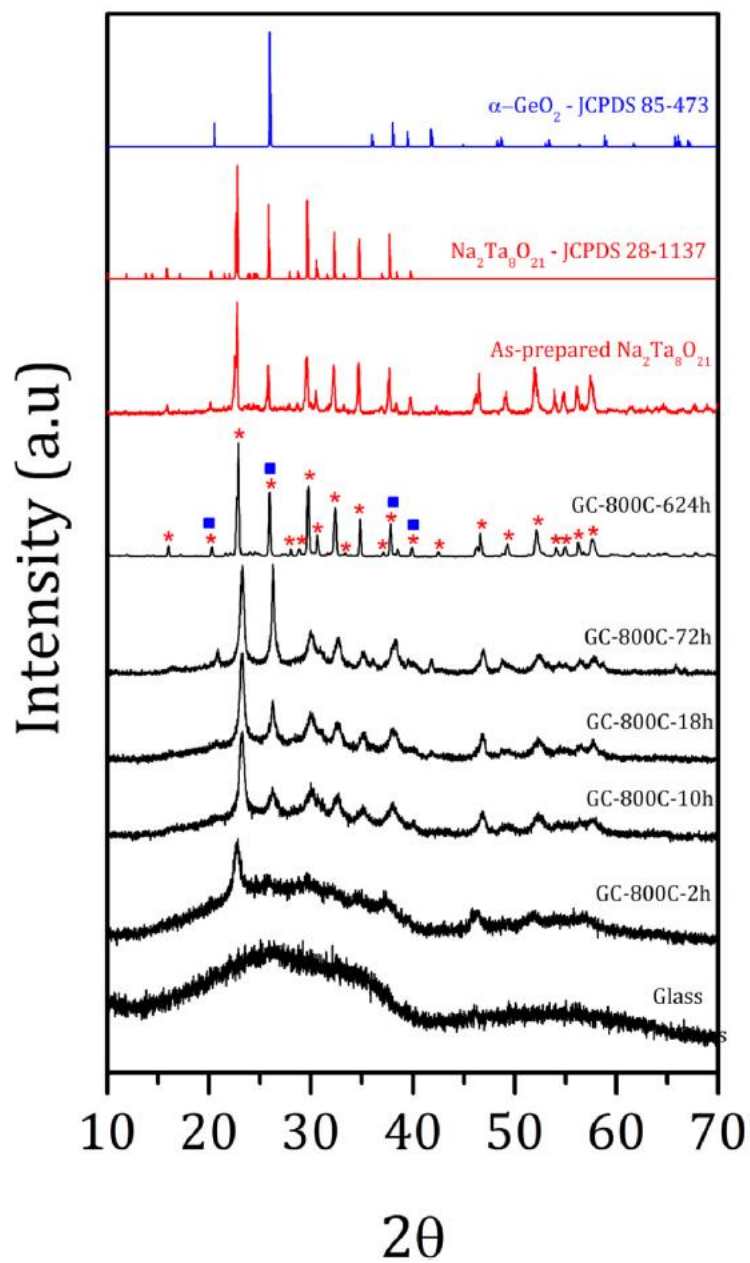


Fig. 2. X-ray diffraction patterns of the pristine glass, glass-ceramics after heat treatment for 2, 10, 18, 72 and 624 h, as-prepared Na₂Ta₈O₂₁ powder, reference JCPDS 28-1137 of Na₂Ta₈O₂₁ and reference JCPDS 85-473 of α-GeO₂.

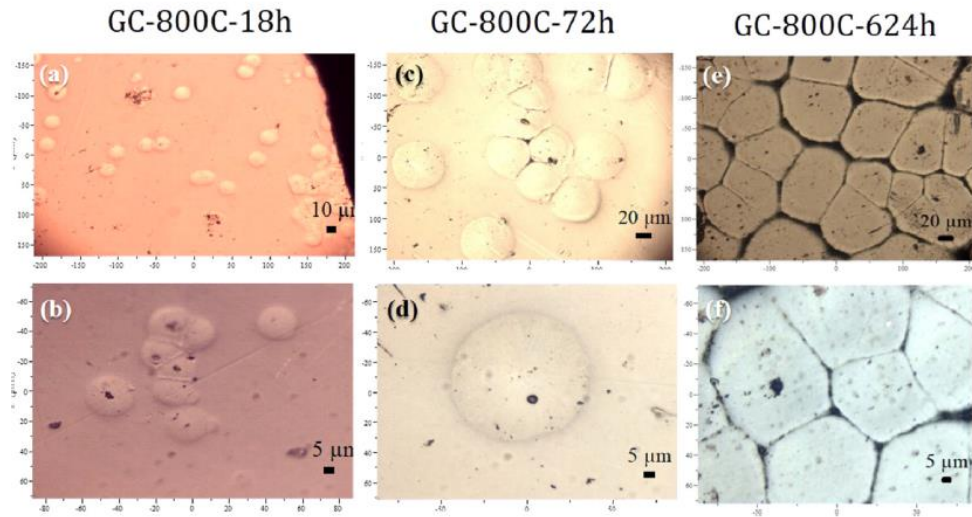


Fig. 3. Optical microscope images of the glass-ceramics surface for a) and b) GC-800C-18 h, c) and d) GC-800C-72 h, e) and f) GC-800C-624 h, showing the spherulites growth and coalescence.

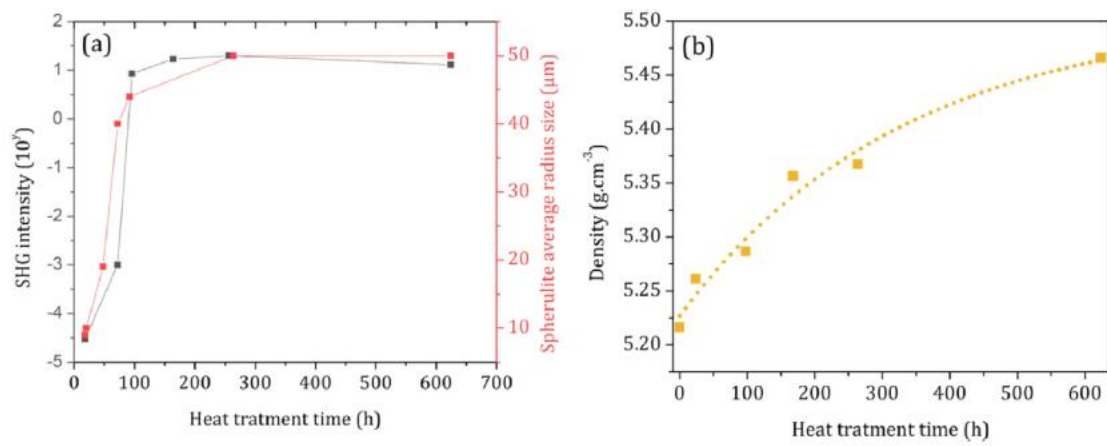


Fig. 4. (a) Spherulite average radius size and SHG relative intensity, (b) density as a function of heat treatment time.

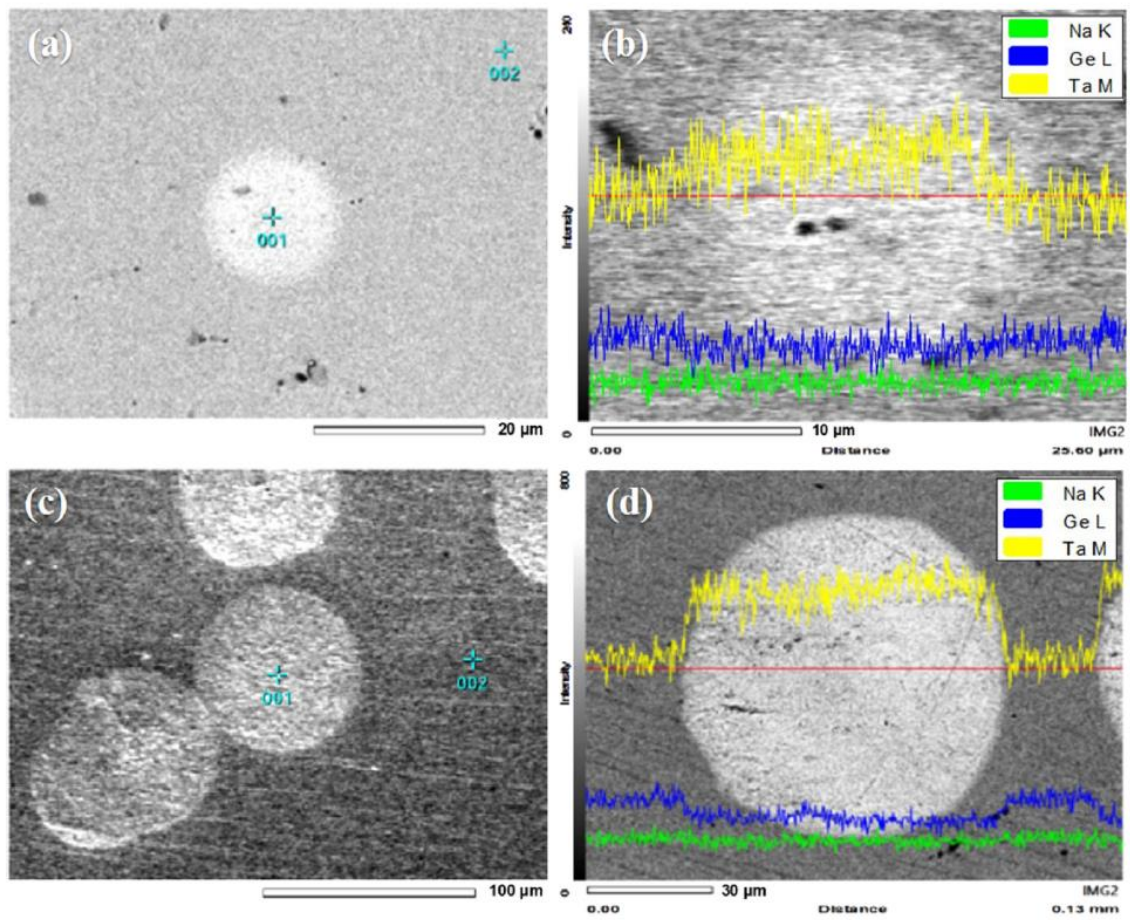


Fig. 5. SEM micrographs on backscattering electrons mode of the samples GC-800C-18 h (a and b) and GC-800C-72 h (c and d), respectively, where a and c present the chosen points for EDS elemental analyzes presented in Table 2 and b and d present the line path chosen (in red) to perform EDS and its elemental analysis of Ta, Ge and Na (intensity profile).

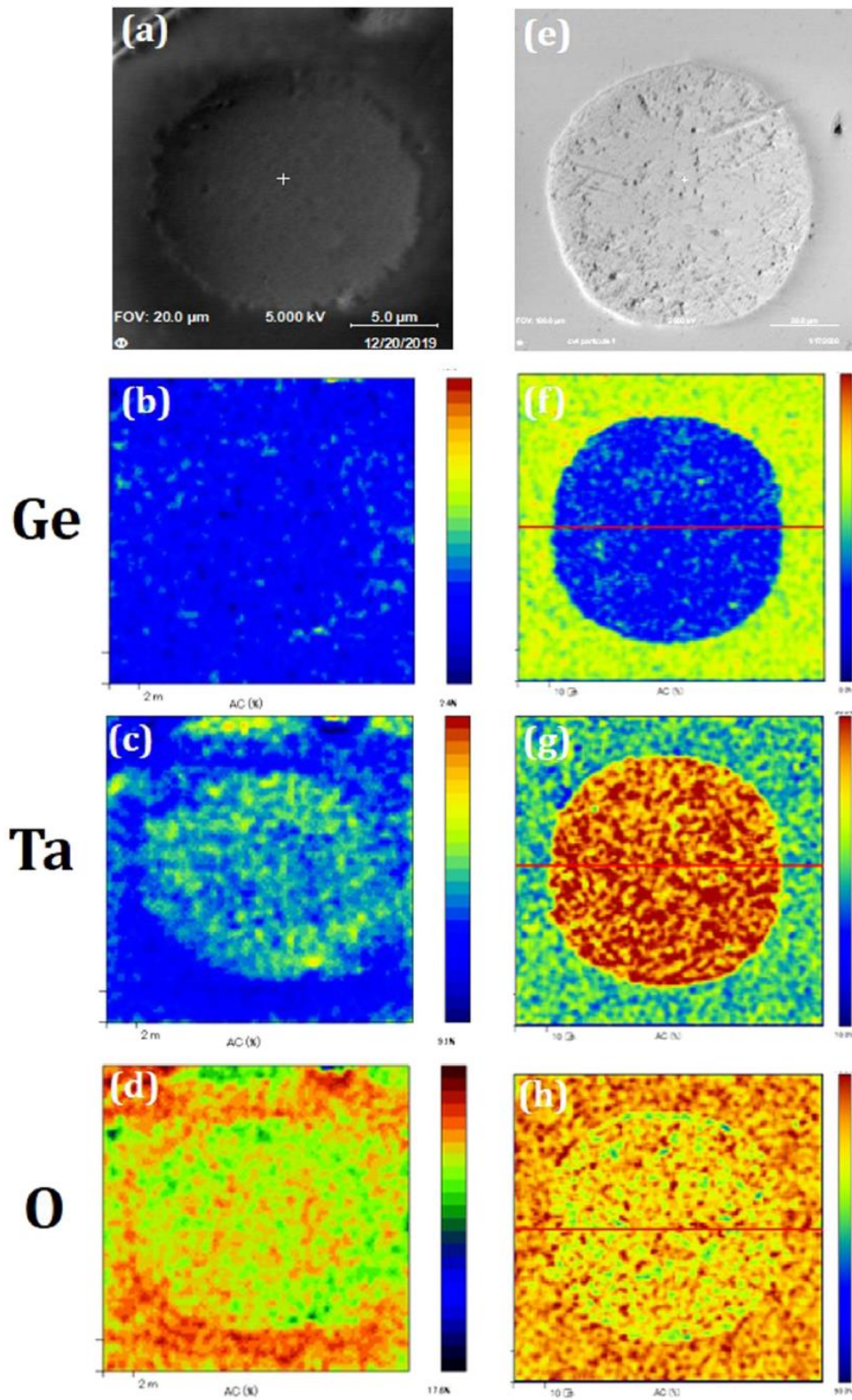


Fig. 6. a) Secondary electron image of a random spherulite for sample GC-800C-18 h analyzed by AES, where b), c) and d) are elemental mappings for Ge, Ta and O, respectively. e) secondary electron image of a random spherulite in GC-800C-72 h, analyzed by AES, where f), g) and h) are elemental mappings for Ge, Ta and O, respectively.

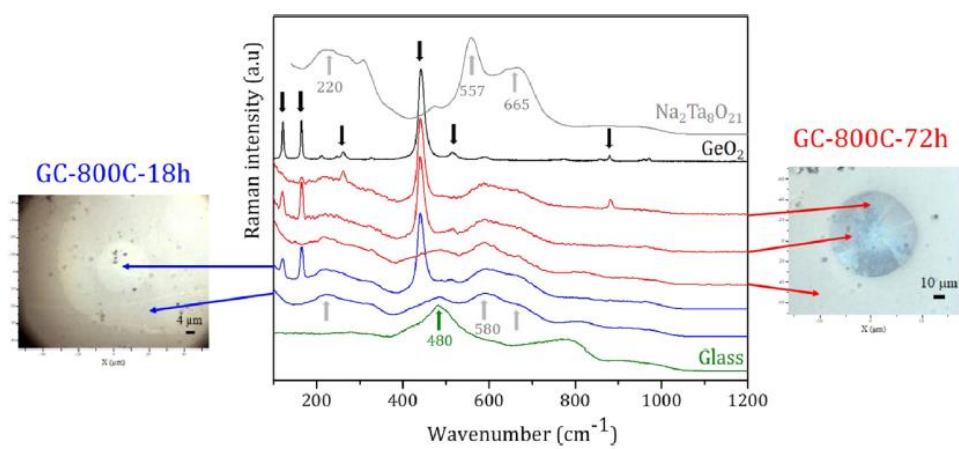


Fig. 7. Raman spectra of crystalline references $\text{Na}_2\text{Ta}_8\text{O}_{21}$, $\alpha\text{-GeO}_2$, pristine glass and representative Raman spectra collected inside and outside of the spherulites for samples GC-800C-18 h and GC-800C-72 h.